ORIGINAL PAPER

Evaluating earthquake-induced widespread slope failure hazards using an AHP-GIS combination

Masanori Kohno[1,2] · **Yuki Higuchi**[3] · **Yusuke Ono**[1,2]

Abstract

Landslides and slope failures are often caused by earthquakes. This study proposes a method to map earthquake-induced slope failure hazards that uses the analytic hierarchy process (AHP) and a geographic information system (GIS) for four districts where many slope failures were induced by earthquakes (the 2018 Hokkaido Eastern Iburi, 2016 Kumamoto, 2008 Iwate-Miyagi Nairiku, and 2004 Mid Niigata Prefecture earthquakes). The assessment system, which was based on the National Research Institute for Earth Science and Disaster Resilience landslide distribution maps, was analyzed using the methods of previously published. We considered the relationships between the earthquake-induced slope failure distributions and landslide hazard factors (elevation, slope angle, slope type, catchment degree, geology, and vegetation). These relationships were utilized for pairwise comparisons of the factors in the AHP analysis. The slope angle, slope type, and catchment degree exerted the highest effects on the slope failure distribution in the four districts. The four earthquake-induced slope failure distributions were highly consistent with the slope failure hazard rank. These results provide a practical method for evaluating earthquake-induced slope-failure hazards.

1 Introduction

Japan is among the most earthquake- and landslide-prone countries worldwide. The geology and topography of the Pacific Ring of Fire, which includes the Japanese archipelago, is rich in magmatic activity, crustal movements, and weathering; moreover, fragile geology and steep topography are widely distributed. Therefore, many slope disasters triggered by earthquakes have occurred in these regions. For example, we

✉ Masanori Kohno
  kohnom@tottori-u.ac.jp; kohnom1103@gmail.com

1 Faculty of Engineering, Tottori University, 4-101, Koyama-Minami, Tottori 680-8552, Japan

2 Center for Regional Management and Safety Engineering, Tottori University, Tottori 680-8552, Japan

3 Graduate School of Sustainability Science, Tottori University, Tottori 680-8552, Japan
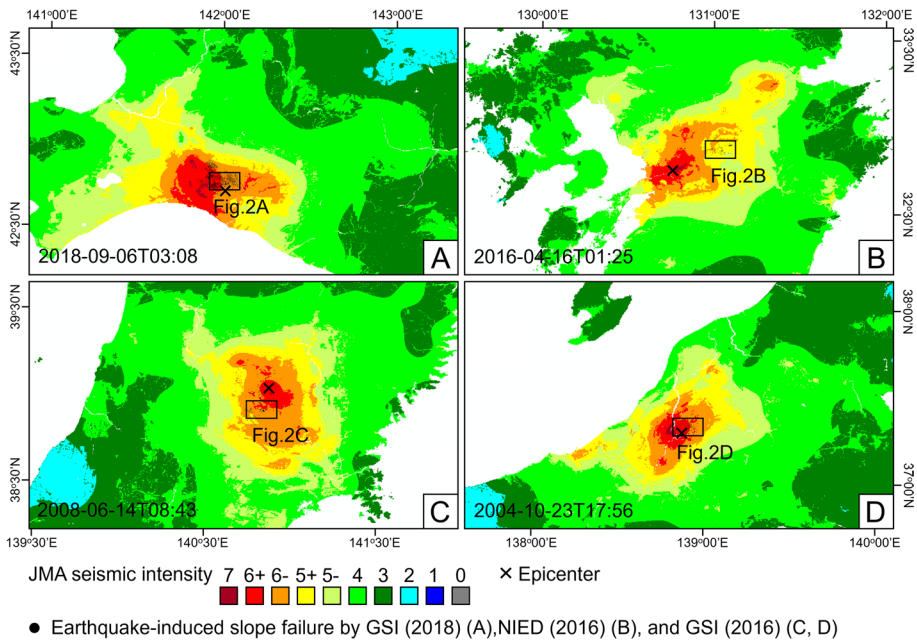
Fig. 1 JMA Seismic intensity distribution of four earthquakes and distribution of earthquake-induced slope failure by AIST (2013). **A** The 2018 Hokkaido Eastern Iburi Earthquake, **B** The 2016 Kumamoto Earthquake, **C** The Iwate-Miyagi Nairiku Earthquake in 2008, **D** Mid Niigata Prefecture Earthquake in 2004. The location of these areas is shown in Fig. 5

Table 1 Information on four earthquakes in this study

Earthquake	Magnitude	Number of earthquake-induced slope failures	Surface geology
The 2018 Hokkaido Eastern Iburi Earthquake[*1]	Mj 6.7[*1]	About 6,000 places[*2]	Tephra[*2]
The 2016 Kumamoto Earthquake[*3]	Mj 7.3[*3]	190 or more places[*4]	Tephra[*4]
The Iwate-Miyagi Nairiku Earthquake in 2008[*5]	Mj 7.2[*5]	2000 or more places[*6]	Tephra[*6]
Mid Niigata Prefecture Earthquake in 2004[*7]	Mj 6.8[*7]	About 4,000 places[*8]	Neogene sediments[*8]

*1 Headquarters for Earthquake Research Promotion (2018), JMA (2004)

*2 Murakami et al. (2019), Umeda et al. (2019)

*3 Headquarters for Earthquake Research Promotion (2016), JMA (2016)

*4 JSECE (2016), MLIT (2016)

*5 Headquarters for Earthquake Research Promotion (2008), JMA (2008)

*6 PWRI (2008), JGS (2010)

*7 Headquarters for Earthquake Research Promotion (2004), JMA (2004)

*8 Niigata Prefecture (2005), Sekiguchi and Sato (2006)

remember the recent 2018 Hokkaido Eastern Iburi earthquake (Fig. 1A and Table 1; epicenter: central-eastern Iburi region, Hokkaido, earthquake magnitude: 6.7, epicenter

depth: 37 km, maximum seismic intensity 7) (Headquarters for Earthquake Research Promotion 2018; JMA 2018; AIST 2013), which occurred at 03:07:59 a.m. on September 6, 2018, which caused widely and densely distributed slope failures (GSI 2018; Murakami et al. 2019; Umeda et al. 2019) (Fig. 2A and Table 1). Immediately after the occurrence of this earthquake, academic research teams from various fields visited the site and performed surveys and field observations of the distribution and damage caused by these slope failures (Yamagishi and Yamazaki 2018; Hirose et al. 2018; Osanai et al. 2019; JGS 2019; JSCE 2019; Tajika et al. 2020; Ishikawa et al. 2021). In addition, many researchers and engineers have conducted surveys and studies (Murakami et al. 2019; Umeda et al. 2019; Kawamura et al. 2019; Kohno et al. 2020a; Li et al. 2020; Wang et al. 2021) to investigate the causes of slope failures and elucidate the mechanisms of their occurrence. In such cases, it is important to clarify the mechanism of the slope failure and thereby establish effective methods, such as risk assessment for slope failure, prediction of the reach of collapsed sediment using numerical analysis, priority evaluation of disaster prevention measures, and others. As shown by the slope failure cases from the 2016 Kumamoto (Fig. 1B and Table 1; Headquarters for Earthquake Research Promotion 2016; JMA 2004; AIST 2013), 2008 Iwate-Miyagi Nairiku (Fig. 1C and Table 1; Headquarters for Earthquake Research Promotion 2008; JMA 2004; AIST 2013), and 2004 Mid Niigata Prefecture earthquakes (Fig. 1D and Table 1; Headquarters for Earthquake Research Promotion 2004; JMA 2008; AIST 2013), the earthquakes that occurred in Japan during the twenty-first century have caused widespread and high-density slope failures (GSI 2018; NIED 2016; JSECE 2016; MLIT 2016; JGS 2010; PWRI 2008; Sekiguchi and Sato 2006; Niigata Prefecture 2005) (Fig. 2B–D and Table 1). Slope failures caused by the above four earthquakes occurred over a widespread area at the time of the earthquakes. In the 2018 Hokkaido Eastern Iburi,
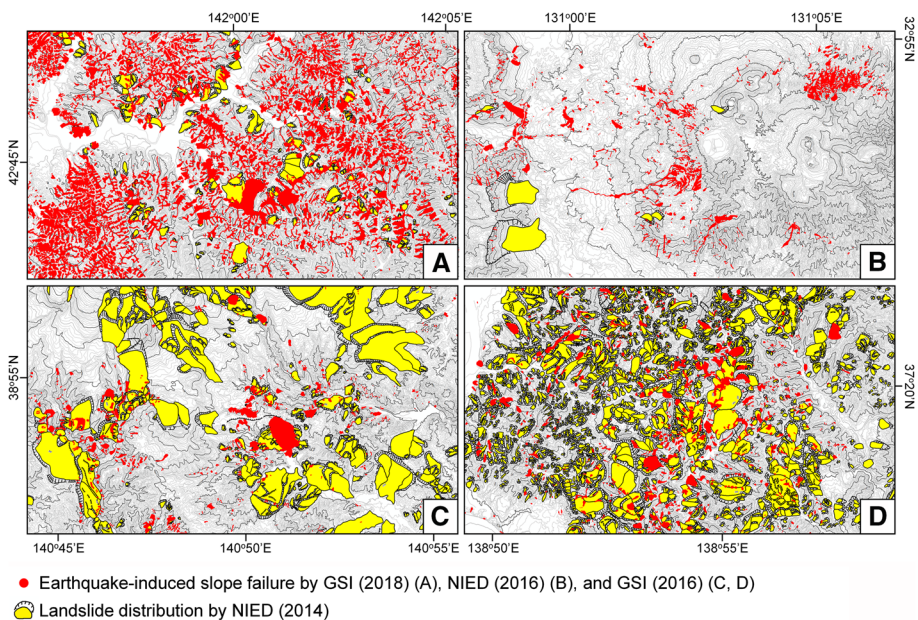

● Earthquake-induced slope failure by GSI (2018) (A), NIED (2016) (B), and GSI (2016) (C, D)

Landslide distribution by NIED (2014)

Fig. 2 Distributions of earthquake-induced slope failures and landslides. **A** The 2018 Hokkaido Eastern Iburi Earthquake, **B** The 2016 Kumamoto Earthquake, **C** The Iwate-Miyagi Nairiku Earthquake in 2008, **D** Mid Niigata Prefecture Earthquake in 2004). The location of these areas is shown in Fig. 5

the 2008 Iwate-Miyagi Nairiku, and 2004 Mid Niigata Prefecture earthquakes, most slope failures occurred in areas with a Japan Meteorological Agency (JMA) seismic intensity between 6+ and 6−. In the 2016 Kumamoto earthquake, most of the slope failures occurred in areas with a JMA seismic intensity between 6− and 5+. Although the damage caused by slope failures due to earthquakes is enormous, it is financially difficult to take preventive measures in all slope-failure risk areas. Therefore, it is necessary to identify slopes with a high risk of slope failure during an earthquake and considering this priority, conduct surveys, implement countermeasures, and perform slope stability analysis. In such cases, one of the first items to consider is topography. In recent years, aerial video surveys using drones (UAVs) have attracted attention and demonstrated their benefits in terms of time and cost when conducting topographical surveys over a wide area (Niethammer et al. 2012; Lucieer et al. 2014; Tanaka et al. 2016; Yamamura et al. 2016; Peternel et al. 2017; Yamasaki 2017; Cui et al. 2020; Ma et al. 2020). However, there are many hurdles to overcome, such as aviation law, radio law, and ordinances. Therefore, as an alternative approach, identifying areas of slope failure hazards from earthquakes objectively using easily available and versatile data can provide useful basic or auxiliary data.

In this study, we first applied the landslide hazard mapping method proposed by Kohno et al. (2020b), which uses an AHP analytic hierarchy process (AHP) analysis and a geographic information system (GIS), to the slope failure distributions (Fig. 2) caused by the above four earthquakes (the 2018 Hokkaido Eastern Iburi, 2016 Kumamoto, 2008 Iwate-Miyagi Nairiku, 2004 Mid Niigata Prefecture earthquakes). Subsequently, the consistency between the landslide hazard rank and slope failure distribution due to the earthquakes was examined. The slope failure due to earthquakes, which was targeted in this study, has different causes and processes compared to landslides. However, a landslide hazard map was first created using the landslide topography distribution, which was then modified by changing the evaluation factors concerning slope failure to map earthquake-induced slope fail hazards. In addition, after confirming the degree of influence of topography, geology, vegetation, etc., on the distribution of earthquake-induced slope failure, we explored the common slope failure evaluation factors among the four earthquakes. Based on the above results, we developed a method to evaluate earthquake-induced widespread slope failure hazards caused by earthquakes using an AHP-GIS combination analysis.

2 Methodology

2.1 Overview of the landslide hazard mapping method by using AHP analysis and GIS proposed by Kohno et al. (2020b)

This section briefly describes the landslide hazard mapping method, using AHP analysis and GIS, proposed by Kohno et al. (2020b). AHP analysis is a decision-making method developed by Saaty (1980) that assigns weights to evaluation factors based on paired comparisons. In the AHP method, the importance weight W_i of each element is generally calculated using the n-th order square matrix A (= $[a_{ij}]$ $_{i,j = 1, 2,...,n}$; paired comparison matrix) [Eq. (1)] of n elements in the evaluation item.

$$A = \begin{bmatrix} a_{ij} & \cdots & a_{in} \\ \vdots & \ddots & \vdots \\ a_{nj} & \cdots & a_{nn} \end{bmatrix} \quad (i, j = 1, 2, \ldots, n) \tag{1}$$

where $a_{ij} > 0$, $a_{ii} = 1$, $a_{ji} = 1/a_{ij}$. The calculation of the weight of each element includes the application of the main eigenvector method, the geometric mean method, and the harmonic mean method. Of these, the geometric mean method is the simplest and the most commonly used method. Furthermore, Kohno et al. (2020b) implemented the geometric mean method to calculate the weights of the elements. The importance weight W_i of each element on the i-th row using the geometric mean method can be calculated by Eq. (2).

$$W_i = \frac{\sqrt[n]{\prod_{j=1}^{n} a_{ij}}}{\sum_{j=1}^{n} \sqrt[n]{\prod_{j=1}^{n} a_{ij}}} \quad (i = 1, 2, \ldots, n) \tag{2}$$

where $\sum W_i = 1$ ($i = 1, 2, \ldots, n$). The consistency of paired comparisons is evaluated using the consistency index [C.I.; Eq. (3)] and the consistency ratio [C.R.; Eq. (4)]. If both are 0.1 or less, the comparisons can be considered to be consistent (Saaty 1980).

$$\text{C.I.} = \frac{\overline{n} - n}{n - 1} \tag{3}$$

where $\overline{n} = \frac{1}{n} \sum_{i=1}^{n} \sum_{j=1}^{n} a_{ij} \frac{W_j}{W_i}$ ($i, j = 1, 2, \ldots, n$).

$$\text{C.R.} = \frac{\text{C.I.}}{\text{R.I.}} \tag{4}$$

where R.I. is the random index that represents the average of random consistency index.

Many previous studies on landslide hazard assessment have utilized AHP analyses (e.g., Miyagi et al. 2004; Yoshimatsu and Abe 2006; Yagi et al. 2009; Hasekioğulları and Ercanoglu 2012; Pourghasemi et al. 2012; Geological Survey of Hokkaido 2013; Mansouri Daneshvar 2014; Roodposhti et al. 2014; Myronidis et al. 2016; Bera et al. 2020). However, the evaluation targets of each study (Miyagi et al. 2004; Yoshimatsu and Abe 2006; Yagi et al. 2009; Geological Survey of Hokkaido 2013) were limited to landslide topography. Thus, these methods primarily focused on reactive landslides. They were also established through brainstorming with several skilled engineers who had conducted landslide surveys for many years. Therefore, they depended largely on the subjective and empirical judgments of the evaluators. Furthermore, the evaluation factors were subdivided, thus requiring advanced technology and additional time. Hence, Kohno et al. (2020b) proposed a new landslide hazard mapping method using AHP analysis. A Frow chart of this method is shown in Fig. 3. In this method, data that are easy to obtain and highly versatile are set as the evaluation factors. In the paired comparison of evaluation factors related to the landslide hazard by AHP analysis, the relationship between the landslide topography distribution (NIED 2014) and the evaluation factors was quantified (ratio between elements in the evaluation factor).

This method first investigates the relationship between the landslide topography and evaluation factors/elements (i.e., the area ratio of both) based on the landslide topography distribution map (NIED 2014) in the target area. The six evaluation factors (hierarchy level 1) related to the landslide hazard by the AHP analysis were elevation, slope angle, slope type, catchment degree, geology, and vegetation, with an emphasis on easy data acquisition and high versatility. A landslide hazard hierarchy system was constructed based on these evaluation factors (Fig. 3A). From this hierarchy system, the importance weight between
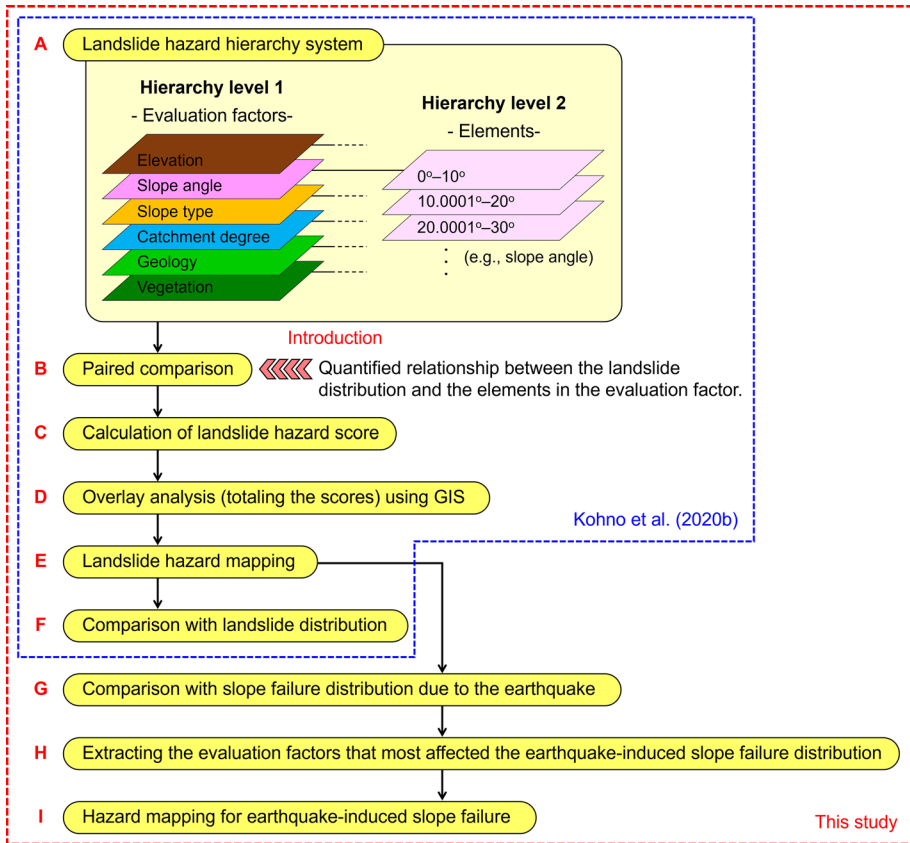
Fig. 3 Frow chart of this study

each element (hierarchy level 2) was first calculated, and then the importance weights among the higher evaluation factors (hierarchy level 1) were calculated. In general, in AHP analysis, the standard scale for paired comparisons when calculating the importance weight of an evaluation factor (or element) is as follows: "equal importance" is 1; "moderate importance" is 3; "strong importance" is 5; "very strong importance" is 7; and "absolute importance" is 9 (2, 4, 6 and 8 are used complementarily). If the importance is low, then the reciprocal is used. Thus, this standard scale inevitably incorporates the subjective and empirical judgments of the engineer. Therefore, in the method by Kohno et al. (2020b), the importance weight was calculated by introducing the quantified relationship between the landslide topography distribution and the elements in the evaluation factor into a paired comparison (Fig. 3B). The landslide hazard level for each evaluation factor was scored based on the obtained importance weights of each layer (Fig. 3C). Landslide hazard mapping was then performed by totaling the corresponding landslide hazard scores for each evaluation factor using GIS (Fig. 3D, E and Fig. 4). This method finally investigates the relationship between the landslide topography and landslide hazard rank based on an obtained landslide hazard map (Fig. 3F). According to the landslide hazard map obtained using this method, the landslide topography distribution ratio tended to increase as the landslide hazard increased. Hence, this method can be expected to extract unstable

Fig. 4 A schematic of the thematic layer overlay analysis using a geographic information system (GIS) to derive landslide slope hazard map
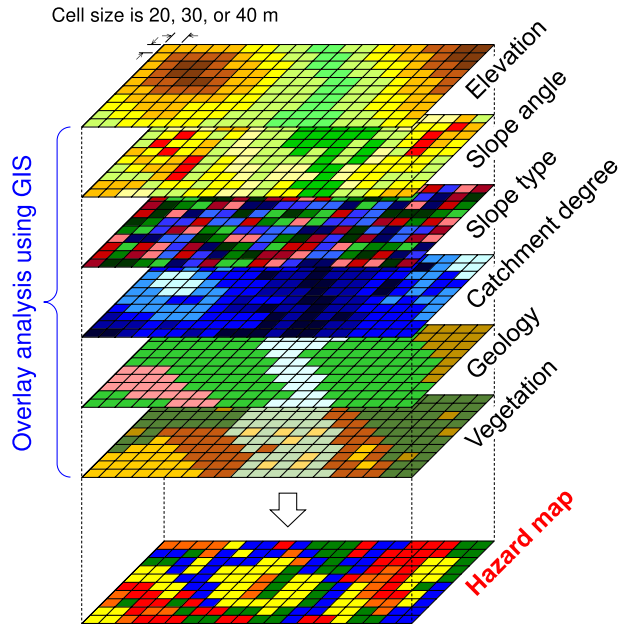
slopes and can contribute to the development of efficient measures, assigning priorities, and slope disaster prevention technology (Kohno et al. 2020b). Therefore, in this study, we proceeded with the study of the earthquake-induced slope failure hazard evaluation method based on the method by Kohno et al. (2020b). That is, the method by Kohno et al. (2020b) was applied to the slope failure area caused by four earthquakes, and subsequent landslide hazard mapping was conducted (Fig. 3A–E; Sects. 2.2–3.3). Furthermore, the obtained landslide hazard map was compared with the slope failure distribution caused by the earthquakes (Fig. 3G; Sect. 3.3). Eventually, the evaluation factors that most affected the slope failure distribution owing to the earthquake were extracted (Fig. 3H; Sect. 4.1), and the results were utilized to repeatedly perform landslide hazard mapping (Fig. 3I; Sect. 4.2). In this study, the validity of the landslide hazard maps was verified using the receiver operating characteristic (ROC) curves and area under the curve (AUC) values (Fawcett 2006), in addition to the relationship between the landslide hazard rank and the distribution of landslides or slope failures. The ROC curves and AUC values are often used to verify landslide hazard maps (e.g., Hasekioğulları and Ercanoglu 2012; Pourghasemi et al. 2012; Roodposhti et al. 2014; Myronidis et al. 2016; Pereira et al. 2017; Bahrami et al. 2021; Salehpour Jam et al. 2021).

2.2 Choosing the research area in this study

In this study, the study area (Fig. 5) was set as the northern Kamuikotan metamorphic, South Kitakami, Joetsu, and Ryoke belt districts, with reference to the geotectonic subdivisions of the Japanese archipelago (AIST 2001; Isozaki et al. 2010). Each of these study areas includes a slope failure distribution area due to one of the above earthquakes. The Kamuikotan metamorphic belt district runs from north to south in central Hokkaido and is a metamorphic belt mainly composed of crystalline schist (Kato et al. 1990). It also
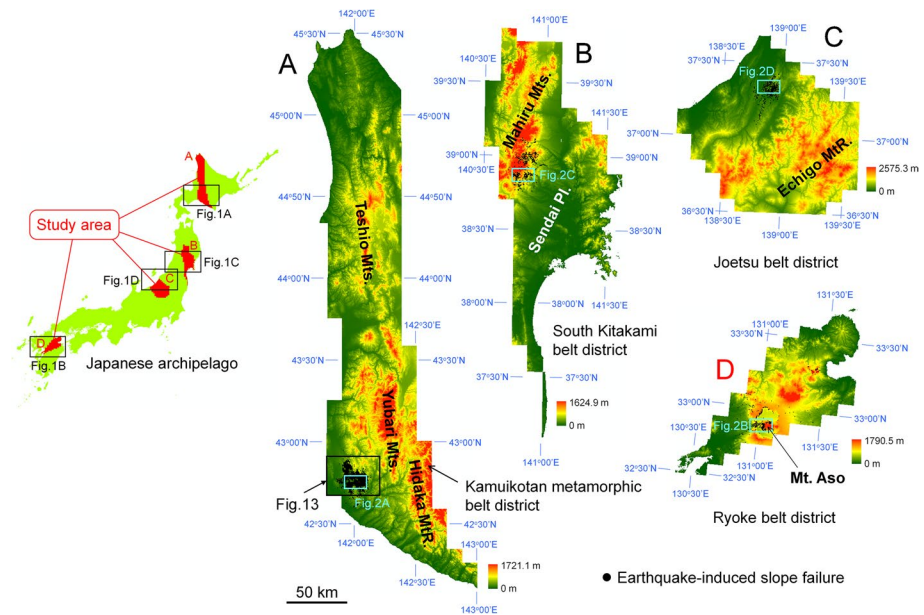
Fig. 5 Location of study areas

has the largest area of serpentinite distribution in Japan, and many landslides and deep-seated landslides have resulted from this serpentinite. The South Kitakami belt district is distributed from the southwestern part of Iwate Prefecture to the northeastern part of Miyagi Prefecture and consists of Pre-Silurian basement rocks (mainly granites) and shallow marine sedimentary rocks (Oide et al. 1989). The Joetsu belt district is distributed from the northwestern part of Gunma Prefecture to the southeastern part of Niigata Prefecture and consists of ultramafic rocks, crystalline schists, hornfelsized schists, and granites (Omori et al. 1986). As shown in Fig. 2D, this area is one of the most landslide-prone regions in Japan. The Ryoke belt district is in the central-eastern part of Kyushu and consists mainly of Ryoke granite and localized Ryoke metamorphic rocks (Karakida et al. 1992).

2.3 Overview of data used in this study

The GIS software used was ArcGIS 10.2.2, from ESRI, Japan. In this study, raster data were used to input and superimpose the landslide hazard scores of each evaluation factor calculated by AHP analysis into each cell of the GIS data model (Fig. 4). The cell size of the raster data was set to 20 m, 30 m, and 40 m, and the degree of influence of the cell size on the analysis results was also examined.

The landslide topography distribution map used the digital archive for landslide distribution maps (SHP format) published by the NIED (2014). This map is a drawing wherein 1:40,000 monochrome aerial photographs taken in the 1970s are topographically interpreted using a simplified actual condition mirror at four magnifications. Furthermore, its outline and basic structure (scarp and moving body) are mapped regarding "landslide topography," which is a topographical trace formed by landslide fluctuation, and its
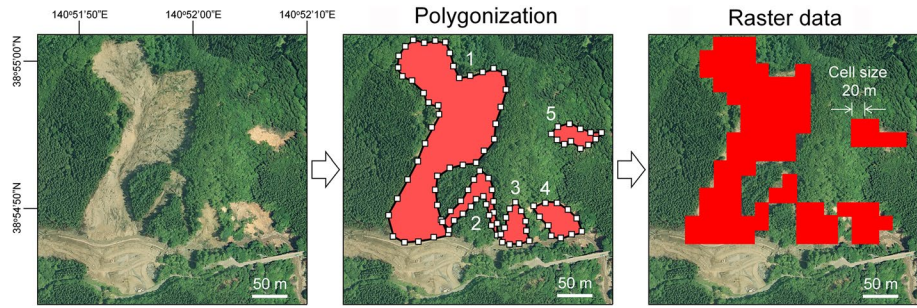
Fig. 6 Delineation of the slope failures and their conversion to a raster data format with a cell size of 20 m

Table 2 Numbers of landslides, earthquake-induced slope failures, and DEM10B files used in this study

District	Number of landslides[1]	Number of earthquake-induced slope failures	Number of DEM10B[2] files
Kamuikotan metamorphic belt district	25,370	5898	225
South Kitakami belt district	5806	1960	137
Joetsu belt district	23,533	1764	117
Ryoke belt district	763	1721	72

[1] NIED (2014)

[2] GSI (2019)

distribution is shown in a 1:50,000 topographic map. However, we did not determine whether the mapped landslide topography occurred because of an earthquake, heavy rain, or other factors. This drawing only presents relatively large landslide areas with a width of ≥ 150 m. Therefore, very small slope fluctuations, such as surface collapse, debris flow, and falling rock, and landslide topography measuring less than 150 m in width, are not subject to interpretation, and no field survey was conducted on the interpreted topography. Therefore, the absence of landslide topography on the map does not indicate the absence of a landslide (NIED 2014). GIS data published by the GSI (2018) were used for the slope failure distribution map for the 2018 Hokkaido Eastern Iburi Earthquake, and the GIS data published by the NIED (2016) were used for the slope failure distribution map for the 2016 Kumamoto Earthquakes. GIS data were obtained from the GSI Maps (GSI 2016) for the slope failure distribution map for the Iwate-Miyagi Nairiku Earthquake and Niigata Chuetsu Earthquake. The outline of the slope failures was directly traced from an aerial photograph [GSI Maps (GSI 2016)] and made into polygons (Fig. 6). Table 2 lists the number of confirmed slope failures caused by the earthquakes in each district. The scale of these confirmed landslide topographies and slope failures due varies in size. Therefore, in this study, the landslide or slope failure topography (vector data) was not treated as a single cell; however, the moving body part (polygon data) of the topography was represented by raster data (Figs. 4 and 6). Naturally, jaggies appear in the outline of the terrain as expressed by the raster. The scalp of the landslide (line data) was not included in the analysis because it did not contain area information.

For topographical data, a digital elevation model (10 m mesh, Digital Elevation Model: DEM10B) of the basic map information published by the GSI (2019) was used. Table 2 lists the number of DEM10B files that comprised each target area. Based on DEM10B, a GIS surface analysis was performed, and elevation, slope angle, slope type, and catchment degree maps of each target area were created. The slope type is an undulating form, Suzuki (1997) in which the unit ground surface is three-dimensionally divided by a combination of the tilt angle of the cell and the change state in the tilt direction. The catchment degree was calculated using GIS surface analysis and Terrain Analysis Using DEM (TauDEM), a topographic analysis tool developed by Tarboton (2006).

For the geological data, we used the Seamless Digital Geological Map of Japan (1:200,000) (Basic version, data update date: 29 May 2015) published by the AIST (2015).

For the vegetation data, we used 1/50,000 Natural Environmental Information GIS (maintained from 1979 to 1998) published by the MOE (1998).

3 Landslide hazard mapping

3.1 Setting the elements (hierarchy level 2)

The above-mentioned six evaluation factors (hierarchy level 1) were classified into each element (hierarchy level 2). The set evaluation factors (elevation, slope angle, slope type, catchment degree, geology, and vegetation) are traditionally considered to be more or less related to each other. However, it is extremely difficult to clarify in detail whether or not these factors are independent of each other when conducting landslide hazard assessments. These factors have often been utilized in previous studies, are closely related to landslides/ slope failures, and represent versatile data. Therefore, these evaluation factors cannot be excluded during landslide hazard mapping. The AHP method assumes that the evaluation factors/elements to be incorporated into the same hierarchy level have high independence. Therefore, in this study, the set evaluation factors were assumed to be independent of each other.

The evaluation factor of elevation was divided into elements from 0 m to 2600 m (the highest altitude in the four areas was 2575.3 m) at intervals of 200 m. The slope angle was divided elements from 0° to 80° at intervals of 10°. The slope type was divided into nine types (convex ridge, rectilinear ridge, concave ridge, convex straight, rectilinear straight, concave straight, convex valley, rectilinear valley, concave valley type slopes) based on the basic classification scheme of Suzuki (1997) (Fig. 7). The catchment degree was divided into five equal classifications. The geological evaluation factors were divided based on the geological age and rock type using the legend of the Seamless Digital Geological Map of Japan (1:200,000) (AIST 2015). The vegetation was divided into 10 categories (I: Natural vegetation in the alpine zone; II: Natural vegetation in the Vaccinio–Piceetea region; III: Substitutional communities in the Vaccinio–Piceetea region; IV: Natural vegetation in the Fagaetea crenate region; V: Substitutional communities in the Fagaetea crenate region; VI: Natural vegetation in the *Camellietea japonica* region; VII: Substitutional communities in the *Camellietea japonica* region; VIII: Riverside, moor, salt marsh, and dune vegetation; IX: Plantation and cultural land; X: Others.) according to vegetation categories I to X of the MOE (1998).

Based on these classifications, the proportion of the landslide topography within the divisions of each factor was investigated. Figure 8 shows an example using the relationship

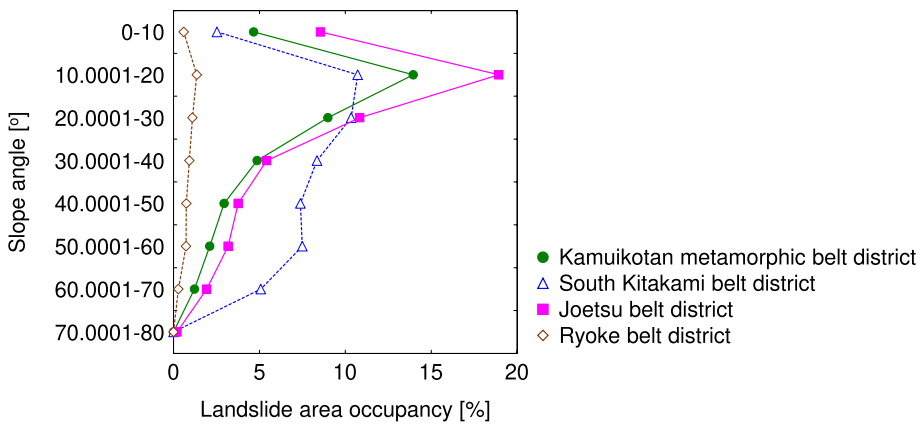**Fig. 7** Basic classification of slope type [Based on Suzuki (1997)]

Fig. 8 An example of the relationship between the landslide distribution and evaluation factors using the slope angle and raster data with cell size of 20 m

between the landslide topography distribution and slope angle at a cell size of 20 m. Landslide areas were most prevalent among all areas at a slope inclination of 10.0001°–20°. When the inclination angle was 20.0001° or greater, the landslide area tended to decrease as the slope angle increased. Therefore, a close relationship exists between the landslide distribution and slope angle. The same tendency was observed for cell sizes of 30 m and 40 m.

3.2 Paired comparisons between evaluation factors (hierarchy level 1) or elements (hierarchy level 2)

First, the paired comparisons between the elements (hierarchical level 2) related to the evaluation factors is explained here using the slope angle (Table 3) with a cell size of 20 m in the Kamuikotan metamorphic belt district as an example. As mentioned above, the numerical value of the standard scale for paired comparison uses the ratio of the landslide occupancy between the elements. For example, the paired comparison values a_{12} in Table 3 for "0°–10°" (4.66%, Fig. 8) and "10.0001°–20°" (13.95%, Fig. 8) are 4.66%/13.95% = 0.33. In contrast, the paired comparison between the "10.0001–20°" and "0°–10°" values is the reciprocal (a_{21} = 13.95%/4.66% = 2.99 in Table 3). Based on this idea, paired comparisons between elements were performed in a similar manner to complete the paired comparison matrix (8-by-8 square matrix; Table 3). The importance weights W_1 to W_8 were calculated by the geometric mean method in Eq. (2). However, since the geometric mean method was used to calculate the importance weights, if no landslide topography was identified ("70.0001°–80°"), the landslide area occupancy in the element was calculated as 1.0×10^{-10}% instead of 0% in the ratio between elements (e.g., a_{18} = 4.66%/1.0×10^{-10}% = 4.7×10^{-10} in Table 3). The order of the importance weights (Table 3) corresponds to Fig. 8. The consistency of paired comparisons was evaluated using the consistency index [C.I.; Eq. (3)] and consistency ratio [C.R.; Eq. (4)]. A C.I. of 0 is considered completely consistent (Saaty 1980). In this study, the ratio between the elements to be paired was used; thus, C.I. = 0 and C.R. = 0.

Second, a paired comparison between the evaluation factors (hierarchy level 1) was performed (Table 4), and the importance weight was calculated. The coefficient of variation of the importance weight of hierarchy level 2 was used as the standard scale for the paired comparisons between evaluation factors at hierarchy level 1. An example of this is shown in Table 4 for a cell size of 20 m in the Kamuikotan metamorphic belt district. For details on setting the standard scale for hierarchy level 1, please refer to Kohno et al. (2020b). The importance weight (0.3602 in Table 3) with a slope angle of 10.0001°–20° was significantly larger than the other elements (0°–10°, 20.0001°–30° to 70.0001°–80°). This means that a slope angle of 10.0001°–20° is closely related to the distribution of landslides. Therefore, the variation in the importance weights of the elements of the slope angle becomes large owing to the influence of the values of the elements in 10.0001°–20°. In other words, if there is a large variation among the importance weights of the elements at hierarchy level 2, the landslide topography is concentrated and distributed based on a specific element. Therefore, the relationship between the evaluation factor and landslide distribution is strong. AHP analysis is an expert system, and hierarchy level 1 paired comparisons must rely on empirical judgments. However, as described above, it may be possible to adequately express the importance of evaluation factors at hierarchy level 1 by using a variation index, such as the coefficient of variation for the relationship of the importance between elements. Therefore, the proposed method is effective. Hence,

Table 3 An example of the pairwise comparisons of evaluation factors, using slope angle, of hierarchy level 2 in the Kamuikotan metamorphic belt district derived using raster data with a cell size of 20 m

	0°–10°	10.0001°–20°	20.0001°–30°	30.0001°–40°	40.0001°–50°	50.0001°–60°	60.0001°–70°	70.0001°–80°	Weight
0°–10°	1	0.33	0.52	0.96	1.59	2.21	3.82	4.7×10^{10}	0.1203
10.0001°–20°	2.99	1	1.55	2.87	4.74	6.61	11.43	1.4×10^{11}	0.3602
20.0001°–30°	1.93	0.64	1	1.85	3.06	4.26	7.37	9.0×10^{10}	0.2321
30.0001°–40°	1.04	0.35	0.54	1	1.65	2.30	3.98	4.9×10^{10}	0.1255
40.0001°–50°	0.63	0.21	0.33	0.60	1	1.39	2.41	2.9×10^{10}	0.0759
50.0001°–60°	0.45	0.15	0.23	0.43	0.72	1	1.73	2.1×10^{10}	0.0545
60.0001°–70°	0.26	0.09	0.14	0.25	0.41	0.58	1	1.2×10^{10}	0.0315
70.0001°–80°	2.1×10^{-11}	7.2×10^{-12}	1.1×10^{-11}	2.1×10^{-11}	3.4×10^{-11}	2.1×10^{-11}	8.2×10^{-11}	1	0.0000
Consistency index C.I.=0, Consistency ratio C.R.=0								Total	1.0000
Coefficient of variation C_v									88.80%

Table 4 An example of the pairwise comparisons of evaluation factors of hierarchy level 1 in the Kamuikotan metamorphic belt district derived using raster data with a cell size of 20 m

	El	Sa	St	Cd	Geo	Veg	Weight
Elevation (El)	1	0.67	0.60	1.80	0.71	0.83	0.1364
Slope angle (Sa)	1.50	1	0.89	2.70	1.07	1.25	0.2043
Slope type (St)	1.68	1.12	1	3.02	1.20	1.39	0.2287
Catchment degree (Cd)	0.55	0.37	0.33	1	0.40	0.46	0.0757
Geology (Geo)	1.40	0.93	0.83	2.52	1	1.16	0.1909
Vegetation (Veg)	1.20	0.80	0.72	2.17	0.86	1	0.1640
Consistency index C.I.=0, Consistency ratio C.R.=0						Total	1.0000

among the indexes showing the variation of data, this study uses the coefficient of variation C_v to set the numerical values of the standard scale for the paired comparisons between the evaluation factors at hierarchy level 1. In addition, if the importance weights of all elements at hierarchy level 2 are the same, the relationship with the landslide distribution is low, and the coefficient of variation C_v is 0. Here, the numerical value ($a_{21}=1.50$ in Table 4) of the paired comparison between the slope angle and the elevation in Table 4 is explained as an example. First, the coefficient of variation C_v of the eight importance weights W_1–W_8 (0°–10° to 70.0001°–80°) of the slope angle can be calculated as 88.80% from Table 3. Similarly, the coefficient of variation C_v of the elevation was 59.30%. The coefficient of variation for the slope angle is larger than that for the elevation; the variation is also large. Therefore, the landslide hazard evaluation is very important. Similar to the paired comparisons at hierarchy level 2, the paired comparison value was set to $a_{21}=1.50$ in Table 4, using the ratio of the two values (80.80%/59.30%). Based on this idea, paired comparisons between evaluation factors (hierarchy level 1) were performed in a similar manner to complete the paired comparison matrix (6-by-6 square matrix; Table 4). Similar to hierarchy level 2, C.I.=0 and C.R.=0.

3.3 Relationship between landslide hazard rank and earthquake-induced slope failure distribution

From the importance weights of each level (evaluation factors and elements), the landslide hazard score $p_{element}$ for each element related to each evaluation factor was calculated using the following formula:

$$p_{element} = \frac{W_1 W_2}{W_{2MAX}} \times 100 \tag{5}$$

where W_1 is the importance weight of each evaluation factor at hierarchy level 1, W_2 is the importance weight of each element at hierarchy level 2, and W_{2MAX} is the maximum value of the importance weight of each element at hierarchy level 2. The landslide hazard score pelement for each element is shown in Table 5. The total of all the landslide hazard scores (overlaid using GIS) for each evaluation factor on a target slope (one cell) was considered the total landslide hazard score P [Eq. (6)].

$$P = \sum p_{element} \tag{6}$$

Table 5 Landslide hazard score (e.g., cell size of 20 m; *Kmb* Kamuikotan metamorphic belt district, *Skb* South Kitakami belt district, *Jb* Joetsu belt district, *Rb* Ryoke belt district)

Evaluation factors	Elements	Kmb	Skb	Jb	Rb
Elevation	0–200 m	2.02	0.49	5.88	3.91
	200.1–400 m	7.43	5.10	13.62	17.81
	400.1–600 m	8.59	9.76	11.00	16.78
	600.1–800 m	7.93	9.13	8.44	21.30
	800.1–1000 m	10.37	10.09	6.69	18.98
	1000.1–1200 m	13.64	11.17	4.67	12.11
	1200.1–1400 m	8.01	11.72	4.87	1.75
	1400.1–1600 m	3.33	7.31	6.15	0.00
	1600.1–1800 m	0.00	0.00	7.90	0.00
	1800.1–2000 m	–	–	5.50	–
	2000.1–2200 m	–	–	2.24	–
	2200.1–2400 m	–	–	0.00	–
	2400.1–2600 m	–	–	0.00	–
Slope angle	0°–10°	6.83	2.57	8.37	6.55
	10.0001°–20°	20.43	10.92	18.51	15.00
	20.0001°–30°	13.16	10.53	10.60	12.16
	30.0001°–40°	7.12	8.51	5.30	10.16
	40.0001°–50°	4.31	7.52	3.68	8.18
	50.0001°–60°	3.09	7.63	3.10	8.01
	60.0001°–70°	1.78	5.17	1.89	3.05
	70.0001°–80°	0.00	0.00	0.19	0.00
Slope type	Convex ridge type slope	22.88	21.29	20.27	22.16
	Rectilinear ridge type slope	1.35	0.75	2.58	3.15
	Concave ridge type slope	22.46	19.25	19.69	21.74
	Convex straight type slope	0.96	0.44	1.37	1.63
	Rectilinear straight type slope	1.03	0.56	0.42	4.63
	Concave straight type slope	1.38	0.59	1.55	3.04
	Convex valley type slope	20.99	19.34	18.50	21.12
	Rectilinear valley type slope	1.12	0.51	1.65	1.36
	Concave valley type slope	22.00	20.56	19.03	22.31
Catchment degree	Class-1	3.80	2.45	16.99	2.79
	Class-2	7.57	3.62	23.39	4.94
	Class-3	6.26	6.84	2.50	5.79
	Class-4	4.55	6.44	1.08	5.43
	Class-5	3.02	5.44	0.00	4.77

Table 5 (continued)

Evaluation factors	Elements	Kmb	Skb	Jb	Rb
Geology	Quaternary sedimentary rocks	0.80	0.68	7.11	4.19
	Quaternary volcanic rocks	0.60	9.76	4.93	5.06
	Neogene sedimentary rocks	4.03	11.2	14.66	9.28
	Neogene volcanic rocks	3.50	16.68	8.45	13.85
	Neogene plutonic rocks	6.59	19.04	5.22	0.00
	Paleogene sedimentary rocks	8.24	–	6.51	16.60
	Paleogene volcanic rocks	–	32.51	–	–
	Paleogene plutonic rocks	0.00	0.00	2.37	–
	Cretaceous sedimentary rocks	8.55	1.04	9.77	8.59
	Cretaceous volcanic rocks	–	0.63	1.69	
	Cretaceous plutonic rocks	–	1.73	2.09	10.32
	Cretaceous accretionary complex	3.98	–	–	–
	Cretaceous metamorphic rocks	–	0.00	–	5.40
	Jurassic sedimentary rocks	8.21	0.24	2.43	–
	Jurassic accretionary complex	10.97	–	3.11	0.00
	Jurassic metamorphic rocks	12.11	–	–	–
	Triassic sedimentary rocks	–	0.34	6.83	–
	Paleozoic sedimentary rocks	–	0.67	6.46	1.29
	Paleozoic accretionary complex	19.09	1.61	5.56	13.00
	Paleozoic plutonic rocks	–	0.00	–	7.38
	Paleozoic metamorphic rocks	–	0.78	0.00	10.02
	Other	1.13	1.62	1.40	9.87
Vegetation	I: Natural vegetation in the alpine zone	13.54	16.73	2.14	–
	II: Natural vegetation in the Vaccinio–Piceetea region	14.56	12.09	5.01	–
	III: Substitutional communities in the Vaccinio–Piceetea region	16.40	12.09	9.54	–
	IV: Natural vegetation in the Fagaetea crenate region	10.82	11.44	4.11	1.99
	V: Substitutional communities in the Fagaetea crenate region	6.76	10.12	6.97	19.01
	VI: Natural vegetation in the *Camellietea japonica* region	0.00	0.49	5.82	8.05
	VII: Substitutional communities in the *Camellietea japonica* region	–	2.05	3.05	6.07
	VIII: Riverside, moor, salt marsh, and dune vegetation	0.39	1.29	3.28	5.41
	IX: Plantation and cultural land	8.40	3.02	6.25	5.67
	X: Others	2.60	0.55	2.82	3.78

Since the score is calculated from the relationship between the element and the landslide

topography, using the AHP method, the total landslide hazard score P naturally depends on the accumulated score of all elements. That is, a high total score indicated a high risk of landslides, and a low total score indicated a low risk. Landslide hazard mapping was performed based on the hazard ranks, and as an example, the total landslide hazard score was classified from I to V (out of $P = 100$ points divided into 5 ranks).

Figure 9 shows a landslide hazard map for each district with a cell size of 20 m. The characteristics of these maps are summarized below. In the Kamuikotan metamorphic belt district, hazard ranks III (41.2%) and IV (49.9%) occupied most of the area. Hazard rank V (3.6%) was distributed harmoniously with the Yubari and Teshio Mountains. Hazard ranks II (4.9%) and I (0.4%) were distributed in localized areas throughout the region. In the South Kitakami belt district, hazard rank IV (20.3%) was harmoniously distributed in the Mahiru Mountains, located in the northwestern and southwestern regions of the Kitakami Mountains. Hazard rank V (0.4%) was distributed within a narrow subsection of the hazard rank IV distribution. Hazard ranks I (9.8%) and II (34.6%) were distributed in the Sendai Plain, which occupies the eastern part of the Mahiru Mountains and southern half of the region. In the Joetsu belt district, the hazard rank IV (72.6%) distribution occupied most of
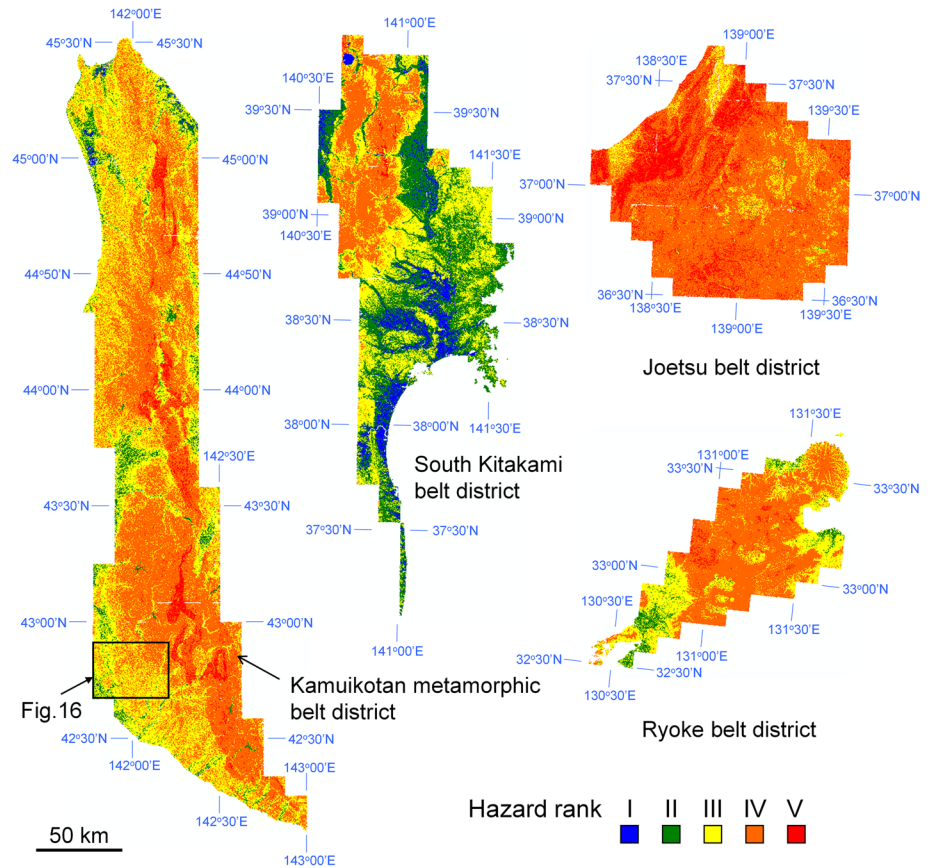
Fig. 9 Representative examples of landslide hazard maps created by the AHP model for the Kamuikotan metamorphic, South Kitakami, Joetsu, and Ryoke belt districts

the area. The hazard ranks III (8.5%) and V (18.8%) were locally distributed. The hazard rank II area (0.1%) was extremely narrow, and hazard rank I was not present. In the Ryoke belt district, hazard ranks IV (61.8%) and III (31.2%) occupied most of the area. Hazard ranks V (2.0%) and II (5.0%) were distributed within a narrow range. Hazard rank I was not present.

Figure 10 shows the relationships between the landslide hazard rank and landslide distribution. In all districts, landslide areas tended to increase as the hazard rank increased. Therefore, a good correspondence was found between the landslide hazard map and the landslide distribution. This was consistent with the tendency shown by Kohno et al. (2020b). The landslide hazard map shown here was verified using the ROC curve and AUC values. The ROC curve (red symbols) demonstrating the relationship between the landslide hazard map (Fig. 9) and landslide distribution is shown in Fig. 11. In addition, the AUC values obtained from the ROC curve are shown in Fig. 12. The ROC curve is a diagram wherein the false positive rate (i.e., 1–specificity) is plotted on the horizontal axis and the true positive rate (sensitivity) is plotted on the vertical axis. It is typically used to evaluate the performance of multiple methods. Values closer to the upper left (the point where a low false positive rate and a high true positive rate are achieved at the same time) signify a better model. The AUC value indicates the quality of the method. The value ranges from 0 to 1, with 1 indicating that complete classification is possible, and 0.5 indicating random classification. The AUC was from 0.76 to 0.83 (Fig. 11), being high in all regions. Further, it can be inferred that it is as high as that in previous studies (Hasekioğulları and Ercanoglu 2012; Pourghasemi et al. 2012; Roodposhti et al. 2014; Myronidis et al. 2016; Pereira et al. 2017; Bahrami et al. 2021; Salehpour Jam et al. 2021) on landslide hazard mapping. Therefore, this result is considered to have the ability to classify landslide hazards. In each district, the characteristics of the landslide hazard maps with a 20 m cell size were approximately the same as those of the 30 m and 40 m cell sizes. Furthermore, the relationship with the landslide topography distribution showed the same tendency, as shown in Fig. 10. In addition, there was no significant difference in the AUC values (Fig. 12) with a change in the cell size. Therefore, when this method is used with a raster data cell size of 20 to 40 m, the actual cell size has almost no effect on the landslide hazard map.

Figure 13 shows the relationships between the landslide hazard rank and slope failure distribution due to the four earthquakes considered in this study. The following trends
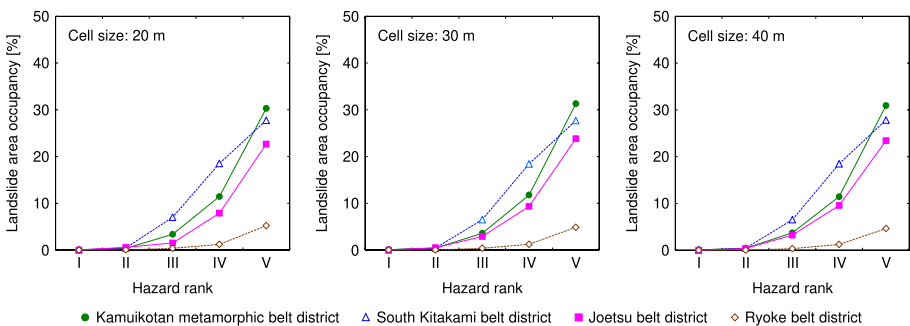

Fig. 10 Percentage of landslide areas in areas with different levels of hazard rank in the landslide hazard maps shown in Fig. 9. The results were derived using raster data with a cell size of 20 m, 30 m, and 40 m, respectively
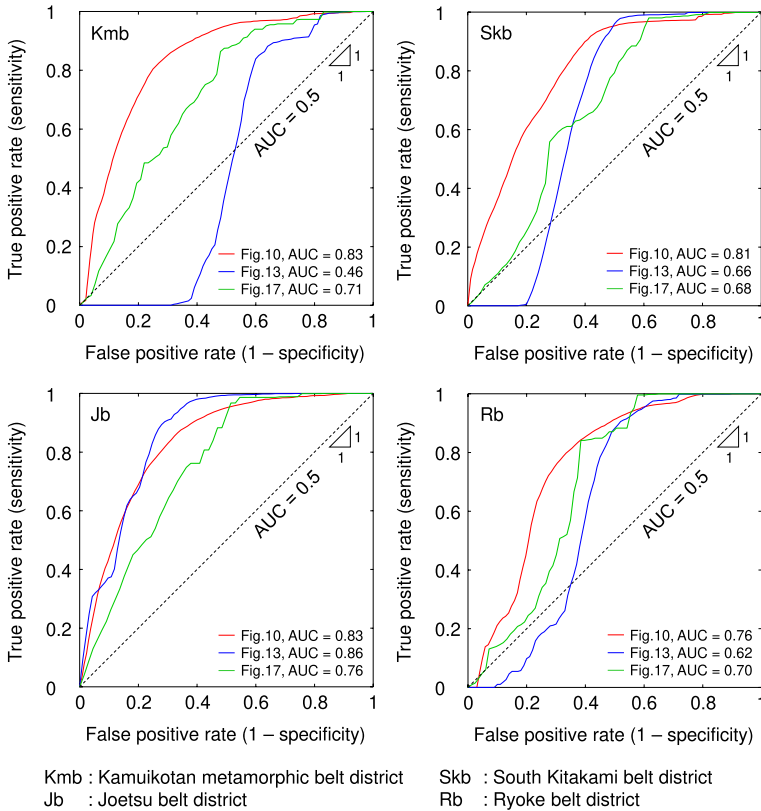
Fig. 11 ROC curves for the AHP model in this study. This figure is related to Figs. 10, 13, and 17. (e.g., cell size of 20 m)
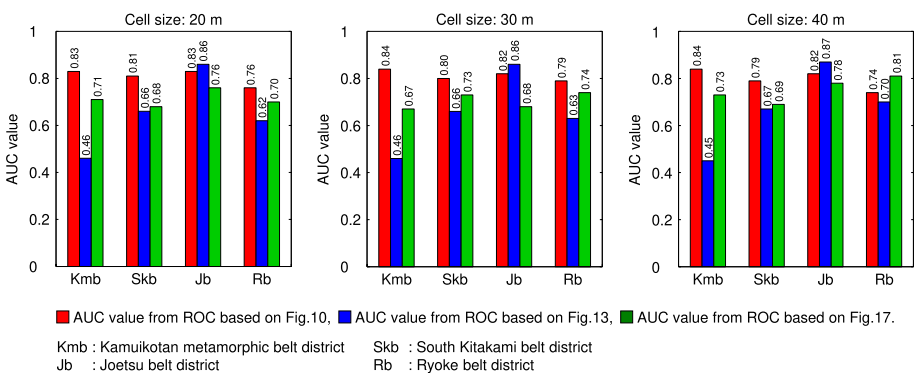

Fig. 12 AUC values obtained from the ROC curve. This figure is related to Figs. 10, 13, and 17

were observed in three of the regions, excluding the Joetsu belt district. In the Kamuikotan metamorphic belt district, the slope failure area due to the earthquake peaked in hazard rank III areas and decreased in hazard rank IV and V areas. In the South Kitakami and Ryoke
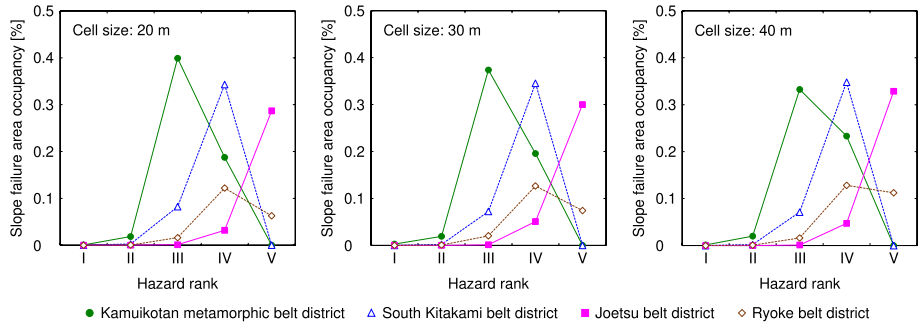
Fig. 13 Percentage of areas with earthquake-induced slope failures in areas with different levels of hazard rank in the landslide hazard maps shown in Fig. 9. The results were derived using raster data with a cell size of 20 m, 30 m, and 40 m, respectively

belt districts, the slope failure peaked in the hazard rank IV areas and decreased in the hazard rank V areas. In contrast, in the Joetsu belt district, good correspondence was found between the landslide hazard rank and slope failure distribution. As mentioned above, this may be because the hazard rank IV areas occupied most of this area. Furthermore, the slope failures caused by the Mid-Niigata Prefecture Earthquake in 2004 were concentrated in the hazard rank V areas. Hence, in the created landslide hazard map, slope failures due to earthquakes did not necessarily occur in the areas where the landslide hazard was high. The ROC in this case is shown by the blue symbols in Fig. 12. All AUC values were lower (AUC = 0.46 to 0.66) than the red symbols except in the case of the Joetsu belt district (AUC = 0.86). In addition, the AUC value was less than 0.5 in the case of the Kamuikotan metamorphic belt district. Therefore, the landslide hazard map created by this method does not properly represent the slope failure distributions caused by the earthquakes.

4 Hazard mapping for earthquake-induced slope failure

4.1 Extracting the evaluation factors that most affected the earthquake-induced slope failure distribution

Among the evaluation factors for the landslide hazard map created in the previous section, we investigated which factor had the greatest effect on the slope failure distributions due to the earthquakes. In this method, the landslide hazard score was calculated with the importance weight of one evaluation factor set at 99.9, and the importance weight of the other five evaluation factors set at 0.02 at hierarchy level 1 in the AHP analysis. Because there were six evaluation factors, six corresponding landslide hazard maps were also created. We thereby confirmed the relationships between the landslide hazard rank in the landslide hazard maps and the slope failure distributions due to the four earthquakes. This makes it possible to understand which evaluation factors affected the earthquake-induced slope failure distributions. In addition, we examined whether the evaluation factors have common characteristics among the four regions. Based on this knowledge, the evaluation factors were narrowed down and set again, and the landslide hazard mapping was performed again, allowing us to examine the relationships between the factors and slope failure distributions due to the earthquakes.
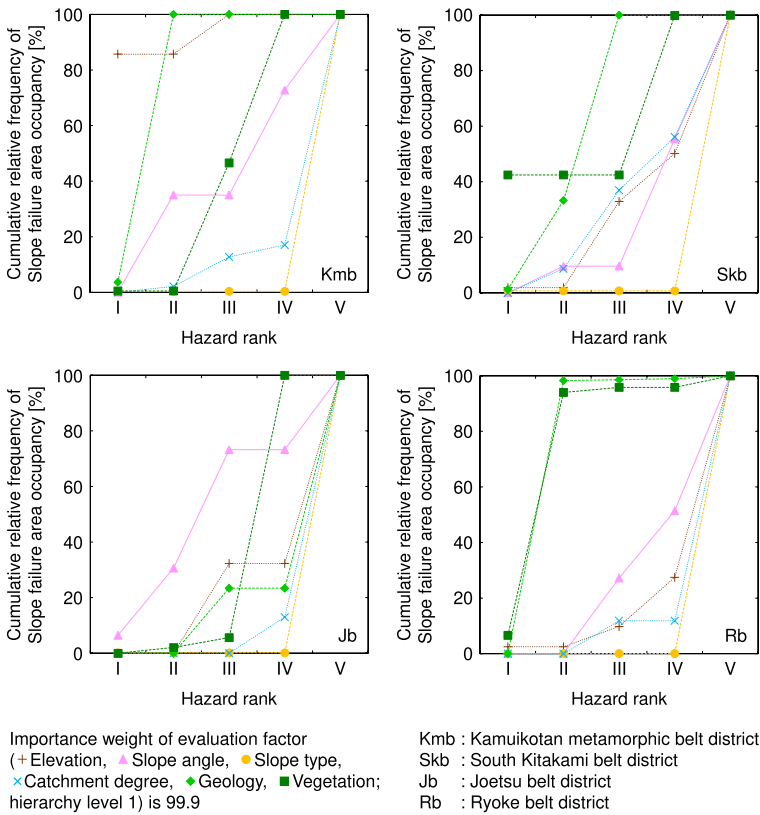
Fig. 14 Percentage of the cumulative relative frequency of slope failure area occupancy in the landslide hazard map when the importance of each evaluation factor (hierarchy level 1) was set to 99.9. The results were derived using raster data with a cell size of 20 m
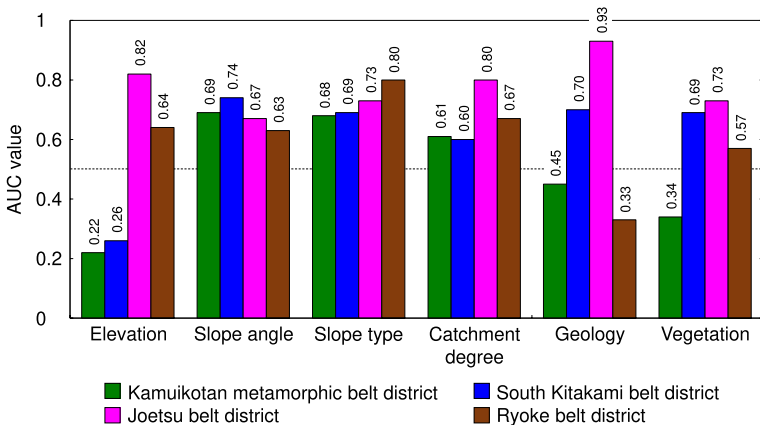

Fig. 15 AUC values obtained from the ROC curve. This figure is related to Fig. 14

Figure 14 shows the relationships between the landslide hazard ranks and the slope failure distributions for the landslide hazard maps that were obtained when the importance weight of each evaluation factor (hierarchy level 1) was set to 99.9. In addition, Fig. 15 displays the AUC values obtained from these ROC curves. In all areas, when the importance weight of the slope type or catchment degree was 99.9, most slope failures to occurred in the hazard rank IV or V areas. Therefore, these two evaluation factors are closely related to the slope failure distributions due to the earthquakes. As per these factors, the AUC values were high in all four districts. That is, when the importance of the slope type is 99.9%, AUC=0.68–0.80, and when the importance of the catchment degree is 99.9%, AUC=0.60–0.80 (Fig. 15). However, in the Kamuikotan metamorphic and Ryoke belt district, for altitude, geology, and vegetation, 80% or more of slope failures occurred in the relatively low-risk hazard rank I and II areas. As per these factors, the AUC values were not high in all four districts, with several districts presenting AUC values less than 0.5 (Fig. 15). Therefore, the involvement of these three factors in the slope failure distribution is not significant. Generally, there is a close relationship between slope failure and geology/vegetation. However, it is probable that their influence was not discernable because the slope failures occurred in areas with the same geology and vegetation in these cases. Regarding the slope angle, approximately 70% of the slope failure occurred in the landslide hazard rank III area in the Joetsu belt district. However, as shown in Fig. 8, the landslide topography was mostly distributed at a specific slope angle (10.0001°–20°) in all areas. In addition, the AUC values (=0.63 to 0.74; Fig. 15) were highly similar, in all four districts. Furthermore, examining many studies (e.g., Osanai et al. 2007; Wakai et al. 2008; Sakai et al. 2013; Hamasaki et al. 2015) on slope failure hazard evaluation due to earthquakes reveals many cases in which the slope angle is mentioned as an evaluation factor. Therefore, we determined that it was not appropriate to evaluate the slope failure hazards due to earthquakes without the slope angle and decided to add it to the evaluation factors.

Hence, landslide hazard mapping was performed again using only three evaluation factors (hierarchy level 1), which were the sum of the slope type, catchment degree, and slope angle, as discussed in the following section. Moreover, all three factors (slope angle, slope type, and catchment degree) are topographic primary causes. As mentioned above, these evaluation factors had similarly high AUC values (Fig. 15) in all four districts. Then, the relationship between this landslide hazard map and slope failure distribution due to the earthquakes was investigated.

4.2 Landslide hazard mapping based on slope angle, slope type, and catchment degree

Based on the methods described in Sects. 2 and 3, landslide hazard mapping was performed using the three evaluation factors. Because all three evaluation factors listed here are common topographic primary causes, the importance weights of the evaluation factors (hierarchy level 1) were all the same. Figure 16 shows an example of these hazard maps (slope failure distribution due to the 2018 Hokkaido Eastern Iburi Earthquake, cell size: 20 m). Hazard ranks II and III were found on the west side of the Atsuma Fault extending in the NNW-SSE direction, and landslide hazard ranks IV and V were found on the east side. As shown in the figure, most of the slope failures occurred in the landslide hazard rank IV and V areas.
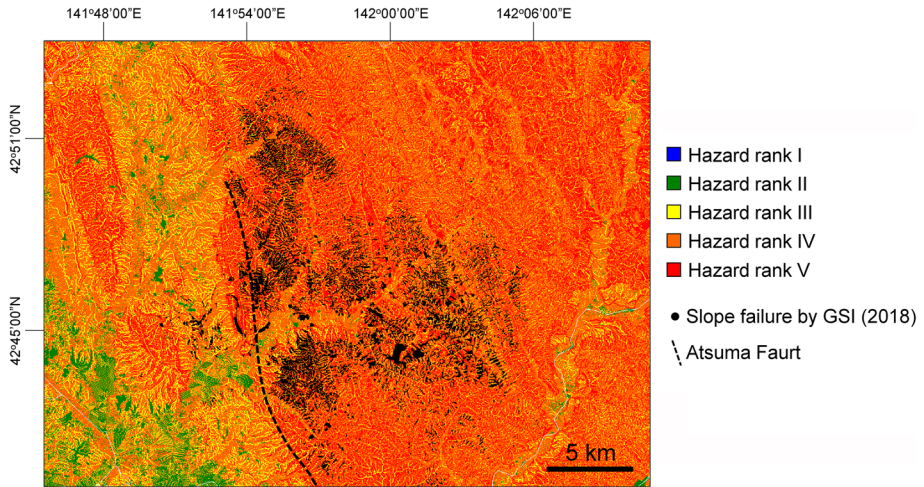
Fig. 16 An example of a landslide hazard map based on slope angle, slope type, and catchment degree, i.e., a part of Kamuikotan metamorphic belt district, which is also shown in Figs. 5 and 9
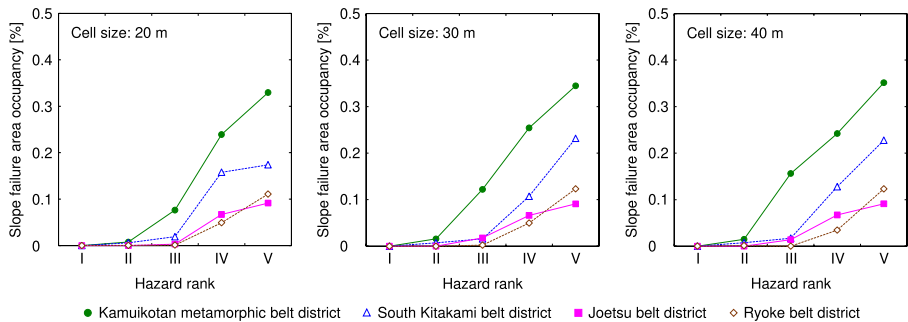

Fig. 17 Percentage of areas with earthquake-induced slope failures in areas with different levels of hazard rank in the landslide hazard maps created by the AHP model, considering slope angle, slope type, and catchment degree. The results were derived using raster data with a cell size of 20 m, 30 m, and 40 m, respectively

Figure 17 shows the relationships between the landslide hazard ranks and slope failure distributions caused by the four earthquakes. In all areas, as the landslide hazard rank increased, the slope failure area tended to increase. The ROC in this case is shown by the green symbols in Fig. 11. Except for the Joetsu belt district, the ROC curve was closer to the upper left than the blue symbols. Furthermore, the AUC value was also higher than the blue symbols. Thus, the landslide hazard maps corresponded well to the slope failure distributions. This is because landslide hazard mapping was performed by collecting and setting only the factors that were closely related to the slope failure distribution. Therefore, evaluating the slope failure hazard due to an earthquake using the slope angle, slope type, and catchment degree is effective. Moreover, this method can be effective for the advance determination of areas with a high risk of slope failure due to sudden phenomena such as earthquakes. In all areas, there was no significant differences in the relationship between the landslide hazard rank and the slope failure distribution due to the earthquake for cell

sizes from 20 to 40 m. Therefore, setting the cell size to 40 m is better for the computational load times of GIS analysis. In developing countries, the accuracy of the topographical data may be low or it may be difficult to obtain data, such as geology and vegetation. Even in such a case, this method, which only requires DEM data of a relatively large 40 m mesh to perform the evaluation, is both advantageous and effective.

5 Conclusions

In this study, we applied the landslide hazard mapping method of Kohno et al. (2020b) to widespread and high-density landslide distribution areas caused by four earthquakes (the 2018 Hokkaido Eastern Iburi, 2016 Kumamoto, 2008 Iwate-Miyagi Nairiku, and 2004 Mid Niigata Prefecture Earthquakes) based on several hundreds to tens of thousands of landslide topographies. Then, the relationship between the landslide hazard ranks and slope failure distribution due to the earthquakes was investigated. Furthermore, the degree of influence of topography, geology, vegetation, etc., on the slope failure distribution was confirmed. Subsequently, we explored the commonalities among the evaluation items for the slope failure distribution and proposed a new earthquake-induced slope failure hazard evaluation method based on the results.

When the method of Kohno et al. (2020b) was used, it was unable to properly express the state of the slope failure distributions during an earthquake. However, the primary topographic causes played major roles in the slope failure distribution during an earthquake. Therefore, it is effective to evaluate the slope failure hazard due to an earthquake using three factors: slope angle, slope type, and catchment degree. We concluded that this method is effective the advance determination of areas with a high risk of slope failure due to sudden phenomena such as earthquakes. In addition, this method has the advantage that the analysis can be performed using only DEM data without the need for other data, such as geology and vegetation. Therefore, it can effectively be applied to areas where data are scarce or inaccurate. Hence, this method can be utilized to locate slopes that will be unstable during an earthquake and require a field survey. Because this method enables efficient priority measurements, we think that it can greatly contribute to the development of slope disaster prevention technology. In future, the relationship between seismic motion and slope failure occurrence mechanism, the spatial correlation between earthquake events and slope failure, and time lag of landslide occurrence after earthquake occurrence will be investigated in detail via time series analysis, and our data can be used for these analyses. By incorporating this information, we aim to improve the accuracy of the method in this study. Furthermore, we plan to further improve this method by exploring its applications and potential in areas subject to various restrictions, such as developing countries.

Declarations

Conflict of interest The authors have no relevant financial or non-financial interests to disclose.

References

Bahrami Y, Hassani H, Maghsoudi A (2021) Landslide susceptibility mapping using AHP and fuzzy methods in the Gilan province. Iran Geojournal 86:1797–1816. https://doi.org/10.1007/s10708-020-10162-y

Bera S, Guru B, Oommen T (2020) Indicator-based approach for assigning physical vulnerability of the houses to landslide hazard in the Himalayan region of India. Int J Disaster Risk Reduct 50:101891. https://doi.org/10.1016/j.ijdrr.2020.101891

Cui Y, Bao P, Xu C, Fu G, Jiao Q, Luo Y, Shen L, Xu X, Liu F, Lyu Y, Hu X, Li T, Li Y, Liu Y, Tian Y (2020) A big landslide on the Jinsha River, Tibet, China: geometric characteristics, causes, and future stability. Nat Hazards 104:2051–2070. https://doi.org/10.1007/s11069-020-04261-9

Fawcett T (2006) An introduction to ROC analysis. Pattern Recogn Lett 27:861–874. https://doi.org/10.1016/j.patrec.2005.10.010

Geological Survey of Hokkaido (2013) Method of landslide activity assessment for risk mitigation. Special Report of the Geological Survey of Hokkaido (**in Japanese**)

Geospatial Information Authority of Japan (GSI) (2016) GSI Maps. https://maps.gsi.go.jp/. Accessed 1 April 2019

Geospatial Information Authority of Japan (GSI) (2018) Distribution map of slope failures and sediments by the 2018 Hokkaido Eastern Iburi Earthquake (GeoJSON format), Information on the 2018 Hokkaido Eastern Iburi Earthquake. https://www.gsi.go.jp/BOUSAI/H30-hokkaidoiburi-east-earthquake-index.html. Accessed 1 April 2019 (**in Japanese**)

Geospatial Information Authority of Japan (GSI) (2019) Digital Elevation Model (DEM10B) (GML format). https://fgd.gsi.go.jp/download/menu.php. Accessed 1 April 2019

Hamasaki E, Higaki D, Hayashi K (2015) Buffer movement analysis and blunder probability analysis for GIS-based landslide susceptibility mapping -a case study of the 2008 Iwate-Miyagi Nairiku Earthquake, Japan. Landslides J Jpn Landslide Soc 52:51–59. https://doi.org/10.3313/jls.52.51 (**in Japanese**)

Hasekioğulları GD, Ercanoglu M (2012) A new approach to use AHP in landslide susceptibility mapping: A case study at Yenice (Karabuk, NW Turkey). Nat Hazards 63:1157–1179. https://doi.org/10.1007/s11069-012-0218-1

Headquarters for Earthquake Research Promotion (2004) Niigata Chuetsu Earthquake on October 23, 2004 (24 October 2004). https://www.jishin.go.jp/main/chousa/04oct_niigata/index-e.htm. Accessed 1 April 2019

Headquarters for Earthquake Research Promotion (2008) Evaluation of The Iwate-Miyagi Nairiku Earthquake in 2008 (26 June 2008) https://www.jishin.go.jp/main/chousa/08jun_iwate_miyagi2/index-e.htm. Accessed 1 April 2019

Headquarters for Earthquake Research Promotion (2016) Evaluation of The 2016 Kumamoto Earthquakes (13 May 2016). https://www.jishin.go.jp/main/chousa/16may_kumamoto/index-e.htm. Accessed 1 April 2019

Headquarters for Earthquake Research Promotion (2018) Evaluation of the 2018 Hokkaido Eastern Iburi Earthquake (12 October 2018). https://www.jishin.go.jp/main/chousa/18oct_iburi/index-e.htm. Accessed 1 April 2019

Hirose W, Kawakami G, Kase Y, Ishimaru S, Koshimizu K, Koyasu H, Takahashi R (2018) Preliminary report of slope movements at Atsuma Town and its surrounding areas caused by the 2018 Hokkaido Eastern Iburi Earthquake. Report of the geological survey of Hokkaido, pp 33–44 (**in Japanese**)

Ishikawa T, Yoshimi M, Isobe K, Yokohama S (2021) Reconnaissance report on geotechnical damage caused by 2018 Hokkaido Eastern Iburi earthquake with JMA seismic intensity 7. Soils Found 61:1151–1171. https://doi.org/10.1016/j.sandf.2021.06.006

Isozaki Y, Maruyama S, Aoki K, Nakama T, Miyashita A, Otoh S (2010) Geotectonic Subdivision of the Japanese Islands Revisited: Categorization and Definition of Elements and Boundaries of Pacific-type (Miyashiro-type) Orogen. J Geogr (Chigaku Zasshi) 119:999–1053. https://doi.org/10.5026/jgeography.119.999 (**in Japanese**)

Japan Meteorological Agency (JMA) (2004) Mid Niigata Prefecture Earthquake in 2004 (No. 31, press released 28 December 2004). https://www.data.jma.go.jp/svd/eqev/data/gaikyo/kaisetsu/kaisetsu20 0412281930.pdf. Accessed 1 April 2019 (**in Japanese**)

Japan Meteorological Agency (JMA) (2008) The Iwate-Miyagi Nairiku Earthquake in 2008 (No. 9, press released 26 June 2008). https://www.jma.go.jp/jma/press/0806/26a/kaisetsu200806261030.pdf. Accessed 1 April 2019 (**in Japanese**)

Japan Meteorological Agency (JMA) (2016) The 2016 Kumamoto Earthquakes (No. 42, press released 31 August 2016). https://www.jma.go.jp/jma/press/1809/20a/kaisetsu201809201500.pdf. Accessed 1 April 2019 (**in Japanese**)

Japan Meteorological Agency (JMA) (2018) The 2018 Hokkaido Eastern Iburi Earthquake (No. 9, press released 20 September 2018). https://www.jma.go.jp/jma/press/1809/20a/kaisetsu201809201500.pdf. Accessed 1 April 2019 (**in Japanese**)

Japan Society of Civil Engineers (JSCE) (2019) Report on the damage surveys and investigations following the 2018 Hokkaido Iburi Tobu and northern Osaka earthquake (**in Japanese**)

Japan Society of Erosion Control Engineering (JSECE) (2016) Emergency reconnaissance report on sediment-related disasters caused by the 2016 Kumamoto Earthquakes (**in Japanese**)

Japanese Geotechnical Society (JGS) (2010) Reconnaissance report on earthquake damage caused by The Iwate-Miyagi Nairiku Earthquake in 2008 (**in Japanese**)

Japanese Geotechnical Society (JGS) (2019) Survey team for geotechnical disasters by the 2018 Hokkaido Eastern Iburi Earthquake. Final reconnaissance report on geotechnical damage caused by the 2018 Hokkaido Eastern Iburi Earthquake (**in Japanese**)

Karakida Y, Hayasaka S, Hase Y (1992) Regional Geology of Japan Part 9: Kyushu. Kyoritsu Shuppan, Tokyo (**in Japanese**)

Kato M, Katsui Y, Kitagawa Y, Matsui M (1990) Regional Geology of Japan Part 1: Hokkaido. Kyoritsu Shuppan, Tokyo (**in Japanese**)

Kawamura S, Kawajiri S, Hirose W, Watanabe T (2019) Slope failures/landslides over a wide area in the 2018 Hokkaido Eastern Iburi earthquake. Soils Found 59:2376–2395. https://doi.org/10.1016/j.sandf.2019.08.009

Kohno M, Noguchi T, Nishimura T (2020b) Landslide hazard mapping in the Chugoku Region using AHP method and GIS. Landslides J Jpn Landslide Soc 57:3–11. https://doi.org/10.3313/jls.57.3 (**in Japanese**)

Kohno M, Joichi T, Ono Y, Noguchi T, Kajikawa Y (2020a) Relationship between earthquake-induced slope failures distribution and topographic primary-cause: A case study of the 2018 Hokkaido Eastern Iburi Earthquake. In: Proceedings of the 10th symposium on sediment-related disasters: pp 213–218 (**in Japanese**)

Li R, Wang F, Zhang S (2020) Controlling role of Ta-d pumice on the coseismic landslides triggered by 2018 Hokkaido Eastern Iburi Earthquake. Landslides 17:1233–1250. https://doi.org/10.1007/s10346-020-01349-y

Lucieer A, Turner D, King DH, Robinson SA (2014) Using an unmanned aerial vehicle (UAV) to capture micro-topography of Antarctic moss beds. Int J Appl Earth Obs Geoinf 27:53–62. https://doi.org/10.1016/j.jag.2013.05.011

Ma S, Wei J, Xu C, Shao X, Xu S, Chai S, Cui Y (2020) UAV survey and numerical modeling of loess landslides: an example from Zaoling, southern Shanxi Province, China. Nat Hazards 104:1125–1140. https://doi.org/10.1007/s11069-020-04207-1

Mansouri Daneshvar MR (2014) Landslide susceptibility zonation using analytical hierarchy process and GIS for the Bojnurd region, northeast of Iran. Landslides 11:1079–1091. https://doi.org/10.1007/s10346-013-0458-5

Ministry of Land, Infrastructure, Transport and Tourism (MLIT) (2016) Sediment disaster by the 2016 Kumamoto Earthquakes. https://www.mlit.go.jp/river/sabo/jirei/h28dosha/h28kumamotojisin.html. Accessed 1 April 2019 (**in Japanese**)

Ministry of the Environment Government of Japan (MOE) (1998) The Natural Environmental Information GIS (SHP format). https://www.biodic.go.jp/trialSystem/top_en.html. Accessed 1 April 2019

Miyagi T, Prasad G B, Tanavud C, Potichan A, Hamasaki E (2004) Landslide risk evaluation and mapping-Manual of aerial photo interpretation for landslide topography and risk management. Report of the National Research Institute for Earth Science and Disaster Prevention, pp 75–137

Murakami Y, Mizugaki S, Nishihara T, Inami Y, Fujinami T (2019) Characteristics of landslides triggered by Hokkaido eastern Iburi earthquake in 2018. Adv River Eng 25:645–650 (**in Japanese**)

Myronidis D, Papageorgiou C, Theophanous S (2016) Landslide susceptibility mapping based on landslide history and analytic hierarchy process (AHP). Nat Hazards 81:245–263. https://doi.org/10.1007/s11069-015-2075-1

National Institute of Advanced Industrial Science and Technology (AIST) (2001) Geology of Japan. https://www.gsj.jp/en/education/geomap-e/geology-e.html. Accessed 1 April 2019

National Institute of Advanced Industrial Science and Technology (AIST) (2013) QuiQuake - Quick Estimation System for Earthquake Maps Triggered by Observed Records. https://gbank.gsj.jp/QuiQuake/QuakeMap/index.en.html. Accessed 1 April 2019

National Institute of Advanced Industrial Science and Technology (AIST) (2015) Seamless Digital Geological Map of Japan (1:200,000) (Basic version, data update date: 29 May 2015) (SHP format). https://gbank.gsj.jp/seamless/index_en.html. Accessed 1 April 2019

National Research Institute for Earth Science and Disaster Resilience (NIED) (2014) Digital archive for Landslide Distribution Maps (SHP format). https://dil-opac.bosai.go.jp/publication/nied_tech_note/landslidemap/gis.html. Accessed 1 April 2019

National Research Institute for Earth Science and Disaster Resilience (NIED) (2016) Distribution map of slope movements by the 2016 Kumamoto Earthquakes (KML format). https://www.bosai.go.jp/mizu/dosha.html. Accessed 1 April 2019 (**in Japanese**)

Niethammer U, James MR, Rothmund S, Travelletti J, Joswig M (2012) UAV-based remote sensing of the Super-Sauze landslide: Evaluation and results. Eng Geol 128:2–11. https://doi.org/10.1016/j.enggeo.2011.03.012

Niigata Prefecture (2005) Mid Niigata Prefecture Earthquake and Sediment Disaster. http://npdas.pref.niigata.lg.jp/sabo/5ec49bc4a1e2b.pdf. Accessed 1 April 2019 (**in Japanese**)

Oide K, Nakagawa H, Kanisawa S (1989) Regional Geology of Japan Part 2: Tohoku. Kyoritsu Shuppan, Tokyo (**in Japanese**)

Omori M, Hayama Y, Horiguchi M (1986) Regional Geology of Japan Part 3: Kanto. Kyoritsu Shuppan, Tokyo (**in Japanese**)

Osanai N, Uchida T, Noro T, Yamamoto S, Onoda S, Takayama T, Tomura K (2007) Application the empirical method of assessing the potential of slope failures to Niigata-ken Chuetsu Earthquake. J Jpn Soc Eros Control Eng 59:60–65. https://doi.org/10.11475/sabo1973.59.6_60 (**in Japanese**)

Osanai N, Yamada T, Hayashi S, Kastura S, Furuichi T, Yanai S, Murakami Y, Miyazaki T, Tanioka Y, Takiguchi S, Miyazaki M (2019) Characteristics of landslides caused by the 2018 Hokkaido Eastern Iburi Earthquake. Landslides 16:1517–1528. https://doi.org/10.1007/s10346-019-01206-7

Pereira S, Garcia RAC, Zêzere JL, Oliveira SC, Silva M (2017) Landslide quantitative risk analysis of buildings at the municipal scale based on a rainfall triggering scenario. Geomat Nat Haz Risk 8:624–648. https://doi.org/10.1080/19475705.2016.1250116

Peternel T, Kumelj Š, Oštir K, Komac K (2017) Monitoring the Potoška planina landslide (NW Slovenia) using UAV photogrammetry and tachymetric measurements. Landslides 14:395–406. https://doi.org/10.1007/s10346-016-0759-6

Pourghasemi HR, Pradhan B, Gokceoglu C (2012) Application of fuzzy logic and analytical hierarchy process (AHP) to landslide susceptibility mapping at Haraz watershed. Iran Nat Hazards 63:965–996. https://doi.org/10.1007/s11069-012-0217-2

Public Works Research Institute (PWRI) (2008) Sediment disaster caused by The Iwate-Miyagi Nairiku Earthquake in 2008. Civ Eng J, pp 34–39 (**in Japanese**)

Roodposhti MS, Rahimi S, Beglou MJ (2014) PROMETHEE II and fuzzy AHP: an enhanced GIS-based landslide susceptibility mapping. Nat Hazards 73:77–95. https://doi.org/10.1007/s11069-012-0523-8

Saaty TL (1980) The analytic hierarchy process: planning setting priorities, resource allocation. McGraw-Hill, New York

Sakai H, Okumura M, Shiwaku T, Kagawa T, Hasegawa K, Sawada S, Tatano Y (2013) A fundamental study on simplified method for calculating earthquake-induced slope collapse ratio. J Jpn Soc Civ Eng Ser A1 (Struct Eng Earthq Eng (SE/EE)) 69:142–147. https://doi.org/10.2208/jscejseee.69.I_142 (**in Japanese**)

Salehpour Jam A, Mosaffaie J, Sarfaraz F, Shadfar S, Akhtari R (2021) GIS-based landslide susceptibility mapping using hybrid MCDM models. Nat Hazards 108:1025–1046. https://doi.org/10.1007/s11069-021-04718-5

Sekiguchi T, Sato HP (2006) Feature and distribution of landslides induced by the Mid Niigata Prefecture Earthquake in 2004, Japan. Landslides J Jpn Landslide Society 43:142–154. https://doi.org/10.3313/jls.43.142 (**inJapanese**)

Suzuki T (1997) Introduction to Map Reading for Civil Engineers Volume 1 -Geomorphological Basis for Map Reading. Kokon Shoin, Tokyo (**in Japanese**)

Tajika J, Amemiya K, Inui T, Toda H, Nishino Y, Takami T (2020) Various internal structures of upheaval zone around terminal part of landslide: a case of tephra slide induced by 2018 Hokkaido Eastern Iburi Earthquake. Landslides J Jpn Landslide Soc 57:84–89. https://doi.org/10.3313/jls.57.84 (**inJapanese**)

Tanaka R, Okabayashi T, Toyama I, Yamamoto K (2016) A proposal of topographical survey by using motion video taken from drone. In: Proceedings of the 8th symposium on sediment-related disasters, pp 61–66 (**in Japanese**)

Tarboton D (2006) Terrain Analysis Using Digital Elevation Models (TauDEM). http://hydrology.usu.edu/taudem/taudem5/. Accessed 1 April 2019

Umeda K, Chiyota K, Shiba M, Kondo M (2019) Landslides triggered by the 2018 Hokkaido Eastern Iburi earthquake. J Jpn Soc Eng Geol 60:172–179. https://doi.org/10.5110/jjseg.60.172

Wakai A, Tanaka N, Abe S, Yoshimatsu H, Yamabe K, Watanabe T (2008) Large-area damage prediction system based on finite element method for risk assessment of seismic slope failure in mountains area. Landslides J Jpn Landslide Soc 45:207–2018. https://doi.org/10.3313/jls.45.207 (**in Japanese**)

Wang F, Zhang S, Li R, Zhou R, Auer A, Ohira H, Dai Z, Inui T (2021) Hydrated halloysite: the pesky stuff responsible for a cascade of landslides triggered by the 2018 Iburi earthquake, Japan. Landslides 18:2869–2880. https://doi.org/10.1007/s10346-021-01656-y

Yagi H, Higaki D, JLS Research Committee for Detection of Landslide Hazardous Sites in Tertiary Distributed Area (2009) Methodological study on landslide hazard assessment by interpretation of aerial photographs combined with AHP in the middle course area of Agano River, Central Japan. Landslides J Jpn Landslide Soc 45:358–366. https://doi.org/10.3313/jls.45.358 (**in Japanese**)

Yamagishi H, Yamazaki F (2018) Landslides by the 2018 Hokkaido Iburi-Tobu Earthquake on September 6. Landslides 15:2521–2524. https://doi.org/10.1007/s10346-018-1092-z

Yamamura M, Uchiyama S, Kumai N (2016) Application of sequential monitoring by UAV-SfM for evaluating deposits of the sediment control dam. Landslides J Jpn Landslide Soc 53:235–239. https://doi.org/10.3313/jls.53.235 (**in Japanese**)

Yamasaki S (2017) Application examples of using drones (UAV) in landslide surveys. *Geol Surv*, pp 27–31 (**in Japanese**)

Yoshimatsu H, Abe S (2006) A review of landslide hazards in Japan and assessment of their susceptibility using an analytical hierarchic process (AHP) method. Landslides 3:149–158. https://doi.org/10.1007/s10346-005-0031-y